

Article

Electroconvection in a Homeotropic Bent-Rod Nematic Liquid Crystal Beyond the Dielectric Inversion Frequency

Pramoda Kumar, Uma S. Hiremath, C. V. Yelamaggad, Axel G. Rossberg, and K. S. Krishnamurthy

J. Phys. Chem. B, **2008**, 112 (32), 9753-9760 • DOI: 10.1021/jp803798g • Publication Date (Web): 23 July 2008

Downloaded from <http://pubs.acs.org> on December 18, 2008

More About This Article

Additional resources and features associated with this article are available within the HTML version:

- Supporting Information
- Access to high resolution figures
- Links to articles and content related to this article
- Copyright permission to reproduce figures and/or text from this article

[View the Full Text HTML](#)

Electroconvection in a Homeotropic Bent-Rod Nematic Liquid Crystal Beyond the Dielectric Inversion Frequency

Pramoda Kumar,[†] Uma S. Hiremath,[†] C. V. Yelamaggad,[†] Axel G. Rossberg,[‡] and K. S. Krishnamurthy^{*,†}

Centre for Liquid Crystal Research, P.O. Box 1329, Jalahalli, Bangalore 560 013, India, and EEP, International Institute for Applied Systems Analysis, 2361 Laxenburg, Austria

Received: April 30, 2008; Revised Manuscript Received: May 29, 2008

We characterize the structural transitions in an initially homeotropic bent-rod nematic liquid crystal excited by ac fields of frequency f well above the dielectric inversion point f_i . From the measured principal dielectric constants and electrical conductivities of the compound, the Carr–Helfrich conduction regime is anticipated to extend into the sub-megahertz region. Periodic patterned states occur through secondary bifurcations from the Freedericksz distorted state. An anchoring transition between the bend Freedericksz (BF) and degenerate planar (DP) states is detected. The BF state is metastable well above the Freedericksz threshold and gives way to the DP state, which persists in the field-off condition for several hours. Numerous +1 and –1 umbilics form at the onset of BF distortion, the former being largely of the chiral type. They survive in the DP configuration as linear defects, nonsingular in the core. In the BF regime, not far from f_i , periodic Williams-like domains form around the umbilics; they drift along the director easy axis right from their onset. With increasing f , the wave vector of the periodic domains switches from parallel to normal disposition with respect to the \mathbf{c} vector. Well above f_i , a broadband instability is found.

Introduction

One of the key material parameters on which the electrical response of a uniaxial nematic liquid crystal depends is the dielectric permittivity anisotropy $\epsilon_a = (\epsilon_{||} - \epsilon_{\perp})$; $\epsilon_{||}$, the permittivity parallel to the preferred axis of molecular orientation, or the director \mathbf{n} , generally displays a relaxation at low frequencies at which ϵ_{\perp} , the permittivity perpendicular to \mathbf{n} , remains steady.¹ This often leads, in nematics for which the static ϵ_a is slightly or moderately positive, to a sign reversal of ϵ_a across the point of dielectric isotropy $\omega_i = 2\pi f_i$. De Jeu et al.^{1,2} were perhaps the first to report a new conduction regime of electroconvection above ω_i in a planar nematic mixture of rod-like molecules. Their experimental phase diagram in the frequency–voltage (ω – V) space depicts, for ω between ω_i and the cutoff frequency ω_c , the primary bifurcation into the Williams domain mode (WDM), leading eventually to the dynamic scattering mode well above threshold. For $\omega > \omega_c$, the dielectric rolls are found. To explain these instabilities, which resemble the low-frequency classical electroconvective instabilities,^{3–6} Goossens⁷ extended the one-dimensional (1-D) Carr–Helfrich–Orsay⁸ theory for the conduction regime by taking into account the complex permittivity $\epsilon_{||} = (\epsilon_{||}' - i\epsilon_{||}'')$. He concluded that $\omega\epsilon_{||}''$ plays the part of anisotropic conductivity, more than the real conductivity anisotropy $\sigma_a = (\sigma_{||} - \sigma_{\perp})$, by which the high-frequency conduction regime, characterized by a static bend distortion and oscillating space charge field just as the low-frequency conduction regime, comes to exist; its width ($\omega_c - \omega_i$) is proportional to ω_q , the charge relaxation frequency or, in effect, $\sigma_{||}$. Threshold conditions for planar two-frequency nematics were also analyzed by Gerber, assuming the instabilities as purely electroconvective.⁹ Later, from a two-

dimensional (2-D) analysis involving all the orientational and electrohydrodynamic terms, Chigrinov et al.¹⁰ inferred the periodic state to be essentially a patterned Freedericksz instability involving no fluid motion. They also reported experimental data on threshold parameters for the planar and homeotropic cases in support of their predictions. In a further development, Chigrinov et al.¹¹ proposed a viscoelastic model to describe the periodic patterns found for a planar nematic in the frequency region near ω_i . They concluded that the body force on ionic impurities and effective space charges generated by dielectric loss sets up a steady cellular motion of small amplitude in a plane transverse to the domain axis, rendering the pattern quasistatic.

Previous experimental work on the instabilities near ω_i for the homeotropic case seems to be limited to a study of the frequency dependence of the critical voltage.¹⁰ Additionally, these studies focus on a few calamitic systems. As far as we know, there has been no report on the electric field effects near the dielectric relaxation region of bent-core systems. We therefore considered it worthwhile to examine the sequence of patterned states for a homeotropically aligned bent-core system near ω_i . Our studies have revealed several new features associated with the secondary instabilities that develop at umbilical sites of the bend Freedericksz (BF) state; the purpose here is to characterize and discuss these in the light of earlier work. Apart from data on dielectric, conductivity, and threshold parameters, the paper includes details of an anchoring transition within the BF state and frequency-induced transformation of pattern geometry.

Experimental Methods

The liquid crystal compound studied here, BCCB, consists of a salicyladimine-based bent-core (BC) mesogen covalently linked, through a hexamethylene spacer, to a rod-like cyano-

* Corresponding author. E-mail: murthyksk@gmail.com.

[†] Centre for Liquid Crystal Research.

[‡] International Institute for Applied Systems Analysis.

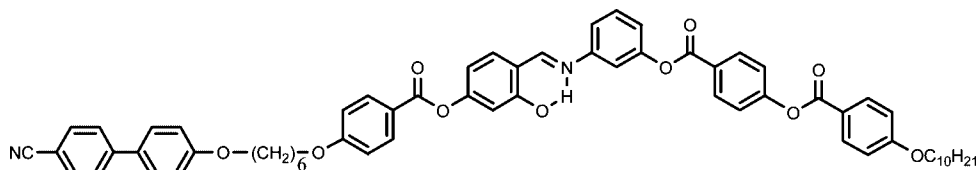


Figure 1. The chemical structure of the twin mesogen (BCCB) used in this study, showing a bent-core unit covalently linked to a calamitic cyanobiphenyl unit.

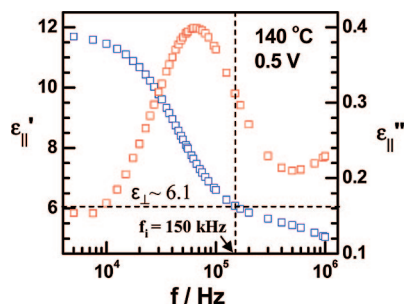


Figure 2. Frequency dependence of the real and imaginary components, $\epsilon_{||}'$ (red squares) and $\epsilon_{||}''$ (blue squares), of the complex dielectric permittivity parallel to the nematic director. 140 °C.

biphenyl (CB) unit. Its chemical structure is shown in Figure 1. The phase sequence of BCCB is reported¹² to be I 162 °C N_b 135.6 °C SmA_b 119.2 °C M 105.5 °C Cr, with I, N_b, SmA_b, M, and Cr denoting isotropic, biaxial nematic, biaxial smectic, uniaxial smectic, and crystal phases, in that order. In our electric field experiments, which concern only the nematic phase, we did not come across any feature that could be ascribed to the conjectured biaxiality. The sample cells were sandwich type, constructed of passivated, ITO-coated glass plates from Delta Technologies. The electrodes were coated with octadecyltriethoxysilane to obtain the homeotropic orientation. Mylar spacers, heat-sealed to the electrodes through cooling from ~250 °C under a uniform pressure, determined the cell spacing, d . The d -value was obtained interferometrically for thin cells, and from cell capacitance measurements for thick cells. The electric field was applied along z , the layer normal. Observations were carried out in transmitted light along z , using a Leitz DMRXP polarizing microscope, equipped with a Mettler hot-stage. The images were recorded using a Sony CCD camera. The voltage source was a Stanford Research Systems DS 345 function generator coupled to a FLC Electronics voltage amplifier (model A800). The applied voltage was measured with a HP 34401A multimeter. For dielectric and conductivity measurements, we employed an Agilent 4284A precision LCR meter. For birefringence measurements, we employed both polarization and two-beam interference fringes formed in a wedge-shaped sample.

For convenience, the polarizer with its transmission axis along x and the analyzer along y , will be represented as P(x)-A(y).

Results and Discussion

A. Electrical Parameters. The electrical parameters relevant to this study are the principal permittivities and conductivities in the relaxation region. Figure 2 presents the typical low frequency dielectric relaxation behavior of $\epsilon_{||}$ at 140 °C, determined from cell-capacitance data on a homeotropically aligned BCCB sample. The dispersion $\epsilon_{||}'(f)$ and absorption $\epsilon_{||}''(f)$ occur over a broad frequency region centered on ~65 kHz. From cell-capacitance data on a planarly aligned sample, ϵ_{\perp} at the same temperature is found to be ~6.1. Thus, the frequency of dielectric isotropy f_i corresponding to 140 °C is ~150 kHz, as indicated in Figure 2.

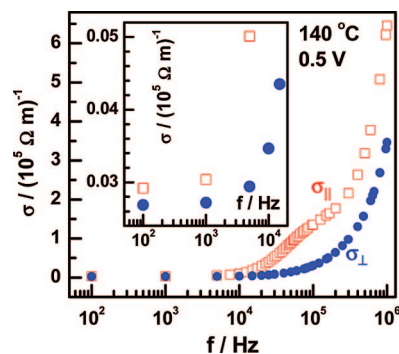


Figure 3. Frequency variation of the principal electrical conductivities $\sigma_{||}$ and σ_{\perp} at 140 °C showing the anisotropy σ_a to be positive in the entire frequency range. The inset is an enlargement of the low-frequency region.

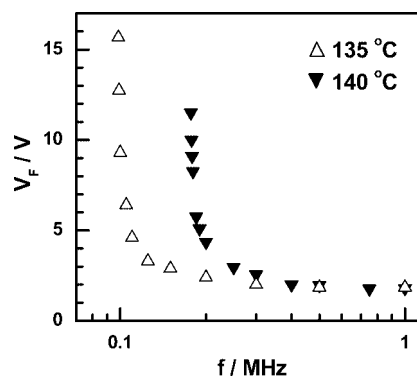


Figure 4. Frequency dependence of the Freedericksz threshold V_F beyond the dielectric isotropy point, for two temperatures.

The frequency variation of the principal electrical conductivities $\sigma_{||}$ and σ_{\perp} at 140 °C, at which most our observations were made, is presented in Figure 3. The conductivity anisotropy $\sigma_a(f)$, which remains positive at all frequencies, ranges between 0.1 $\mu\text{S m}^{-1}$ and 0.18 $\mu\text{S m}^{-1}$ in the frequency region 0.1–0.6 MHz in which the instabilities are investigated.

The charge relaxation frequency corresponding to the components of conductivity and permittivity along \mathbf{n} , $f_q = \sigma_{||}/(\epsilon_o \epsilon_{||})$, as inferable from Figures 2 and 3, increases considerably with f in the dielectric relaxation region. Using the real component of the complex permittivity in arriving at f_q , we find it, at 140 °C, to scale from ~0.23 MHz at $f = 0.1$ MHz to ~0.8 MHz at $f = 0.6$ MHz.

B. Bend-Freedericksz Transition. Under conoscopic observation, between crossed polarizers, a homeotropically aligned BCCB sample shows a centered uniaxial figure. It remains orientationally unperturbed in low frequency fields. Beyond the dielectric inversion point, the primary bifurcation into the BF state takes place. The threshold voltage of this transition, given by $V_F = \pi[k_{33}/(\epsilon_o \epsilon_a)]^{1/2}$ with k_{33} as the bend elastic modulus,^{3–6} may be expected to diverge as f approaches f_i from well above the inversion point. Figure 4 shows the $V_F(f)$ curves for two temperatures.

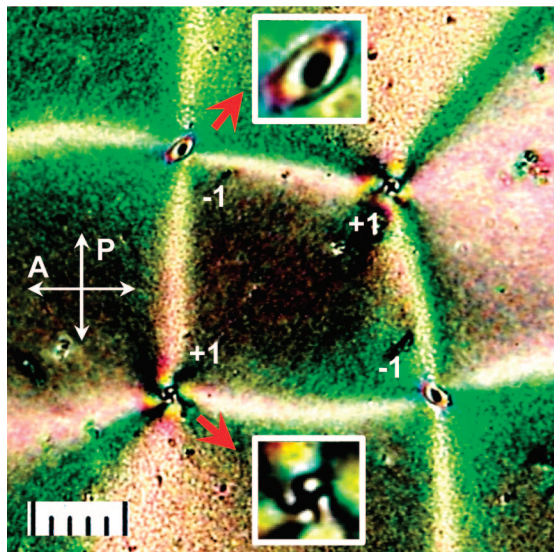


Figure 5. A typical network of alternating +1 and -1 umbilics formed in the BF state of nematic BCCB at 140 °C. $d = 19.3 \mu\text{m}$. Scale division 10 μm .

At the Freedericksz transition, the rotational symmetry of the basic state in the layer plane is spontaneously broken, and the inplane director \mathbf{n}_\perp , representable in terms of the tilt amplitude S and unit vector \mathbf{c} by $\mathbf{n}_\perp = S(x,y,z) \mathbf{c}(x,y)$, displays an infinite degeneracy leading to the so-called Goldstone mode. Optically, this state manifests as a network of alternating +1 and -1 umbilics. We may recall here that the \mathbf{c} field for a +1 umbilic may be either purely radial or tangential. These types are designated correspondingly as *c*-splay and *c*-bend (or chiral or twist) umbilics.⁶ While the linear energy density of a -1 umbilic varies as $(k_{11} + k_{22})/2$, k_{11} and k_{22} denoting the splay and twist elastic moduli, respectively, that of a +1 umbilic is proportional to k_{11} for the *c*-splay case and to k_{22} for the *c*-bend case.^{13a} Energy-wise, therefore, chiral umbilics are to be favored over splay umbilics as long as $k_{22} < k_{11}$, which usually is the case. Experimentally, splay, twist, and mixed splay-twist umbilics have been observed under various conditions.^{13b} In BCCB, +1 umbilics are predominantly of the chiral type far from the core, as evident from the nature of periodic patterns developed in the umbilical regions (see Section C). This is also indicated at a +1 umbilical site, when using a single polarizer, by the strong intensity modulations observed along the normal to the incident vibration direction because of thermal fluctuations of \mathbf{n} . In the core-region, however, splay-twist type director distributions are not uncommon; this aspect is revealed in Figure 5 by the spiral-like appearance of the corresponding extinction brushes. The texture in Figure 5, recorded at $\sim 5V_F$, corresponds to a highly distorted state in which the \mathbf{c} vector is, in general, nonuniform across the sample thickness, for a given (x, y) . This is indicated by the appearance of birefringence at the site of extinction brushes seen at lower voltages. The textures in Figure 6 obtained at different voltages clearly demonstrate this aspect. The absence of Maltese crosses at -1 umbilics in Figure 5 is perhaps to be attributed to the twist of the \mathbf{c} vector about z in the region surrounding the core.

C. Anchoring Transition. Close to f_i , for a voltage $\sim 2V_F$, the BF state becomes metastable. In time, there follows an anchoring transition into a degenerate planar (DP) state in which the molecules tend to lie parallel to the bounding surfaces (or the xy plane), but without a preferred azimuthal direction. The DP domains grow through front-propagation, as illustrated in Figure 7; as may be seen in panel (b), the front involves a

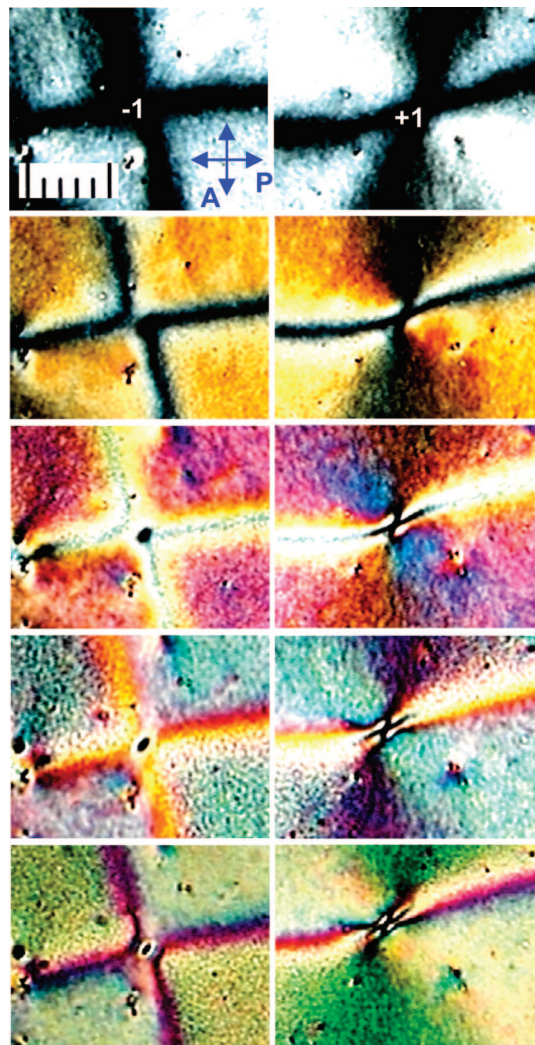


Figure 6. Increasing birefringence colors seen with voltage rise, at the site of +1 (right column) and -1 (left column) umbilics. P(x)-A(y). 300 kHz. For the frames from top to bottom, the voltages are 6.7, 9.5, 11.7, 13.9, and 17.2 V. $d = 19.3 \mu\text{m}$. $V_F = 5.3$ V. Scale division 10 μm .

disclination line and it is possible to think of it, for example, as a $-1/2$ line. The corresponding director field is shown in the inset to Figure 7b. The propagation speed of the front, deduced from a video recording, using a $18.9 \mu\text{m}$ thick sample at 140 °C subject to a 350 kHz, 12.3 V field, is $\sim 1.5 \mu\text{m/s}$. Far from f_i , the transition to the DP state occurs at a much greater voltage relative to the corresponding V_F ($\sim 10V_F$ for 400 kHz, 140 °C). These estimates are for the nucleation of the DP domains within a few minutes of applying the voltage.

It is important to recall here a recent report¹⁴ on a planarly aligned calamitic-bent-core nematic exhibiting an electric-field-induced transition from the uniaxial phase N_u into what is described as the biaxial phase N_b . There again the ground-state is altered after the field is switched off from the N_b state. But most importantly, the birefringence of the second phase is lower than that of the first, and this is used as the main evidence for the identification of the N_b phase. We may now examine the relative birefringence in the two states of BCCB. The birefringence $\Delta n = (n_e - n_o)$ for mercury green light measured by the wedge method as a function of temperature T is shown in Figure 8; at 140 °C, Δn is 0.167. In the BF state, with $V = 9.7$ V, $f = 0.2$ MHz, and $T = 140$ °C, a $16.8 \mu\text{m}$ thick sample displays the first order indigo-blue between crossed polarizers in the diagonal

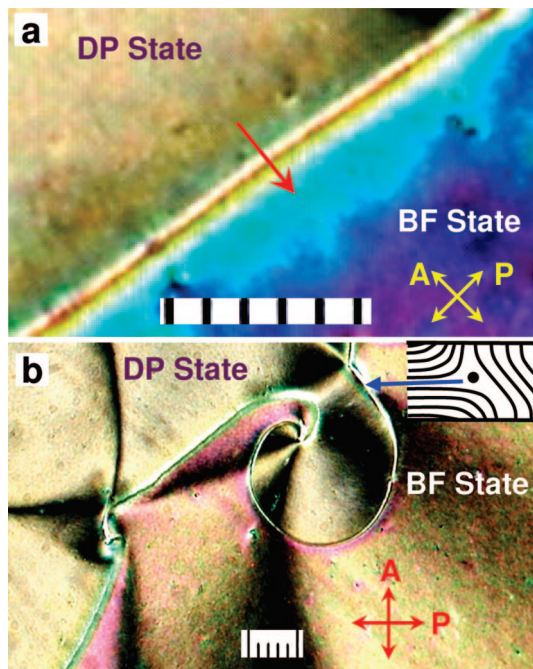


Figure 7. Transition from the metastable BF to DP state in a $16.8 \mu\text{m}$ thick sample at 140°C , for (a) 200 kHz , 9.7 V and (b) 250 kHz , 10.5 V . The red arrow in panel (a) indicates the propagation direction of the invading DP front. In panel (b), the invading front is winding around an umbilic, and a disclination line is discernible in the transition region. A possible structure for the disclination is depicted in the inset at the top right in panel (b). Scale division $10 \mu\text{m}$.

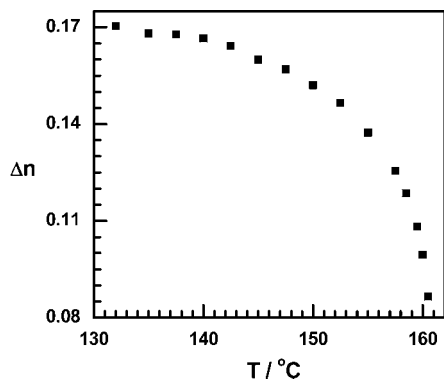


Figure 8. Temperature variation of birefringence of BCCB for mercury green light.

position with respect to c (Figure 7a). The corresponding path difference determined using a tilt compensator is $0.61 \mu\text{m}$. After transformation into the second phase, the color rises to the fourth-order pale pink corresponding to a retardation of $2.55 \mu\text{m}$ or birefringence of 0.152 . This is $\sim 9\%$ lower than the value expected for a planar sample. Considering the slight thickness variation possible over the sample area, it is reasonable to interpret the sharp rise in birefringence as due to the transition to planar anchoring. It is relevant to add here that we found no evidence of any twist between the top and bottom planar alignments in the DP state. The locally planar zones could always be extinguished between suitably oriented crossed polarizers, and this would not be possible in general with a twisted nematic in view of its “wave guiding” property.⁶

After the field is turned off, the BF domains return to the initial homeotropic state with no significant delay; the DP domains, by contrast, take several hours before completely transforming to the initial state through a slow regression of

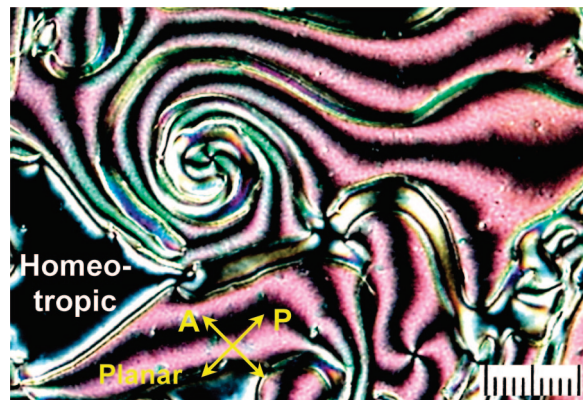


Figure 9. Texture soon after switching the field off from a state of coexistence of BF and DP domains; in the BF region, the initial homeotropic alignment is fully recovered while the DP region persists in the off state. $d = 14.7 \mu\text{m}$. 135°C . Scale division $10 \mu\text{m}$.

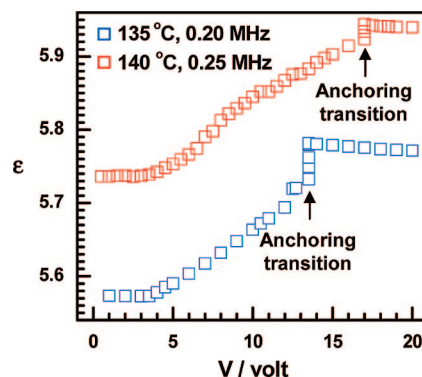


Figure 10. Voltage variation of dielectric constant for an initially homeotropic layer of BCCB, with temperature and field frequency as constant parameters.

the front between the DP and homeotropic regions; even the wall defects formed in this state survive for long in the off state (Figure 9). By applying a suitable low-frequency field, as for example with $f = 1 \text{ kHz}$ and $V = 15 \text{ V}$, the metastable DP domains could be induced to relax to the base state almost immediately.

The anchoring transition just described is also reflected in $\epsilon(V)$ and $\sigma(V)$ measurements. For example, with progressive increase in voltage, the dielectric constant, which is ϵ_{\parallel} below the Fredericksz transition, is expected, above V_F , to increase smoothly approaching the saturation value ϵ_{\perp} .¹⁵ However, as depicted in Figure 10 for frequencies $f > f_i$ and two different temperatures, ϵ exhibits a steep rise around $3V_F$ to reach a near saturation value. This occurrence coincides with the optical transition into the highly birefringent state. A corresponding behavior is seen in Figure 11 showing the voltage dependence of σ .

D. Secondary Bifurcations within the BF State (Phase 1).

Figure 12 is a schematic of the phase diagram for the BF state. In the frequency region 1 of this Figure, wherein ϵ_a is very small and negative, raising the voltage well above V_F drives the sample back to the ground-state because of dielectric heating and reversal of the sign of ϵ_a consequent on an upshift of f_i . Around $10\text{--}15 \text{ kHz}$ above f_i , in region 2, a secondary bifurcation into a patterned state occurs at $V \approx 4V_F$. The pattern around a $+1$ umbilic consists of radial focal lines (R stripes). They are formed as a result of a periodic splay–bend distortion of the director, with its c vector normal to the rolls or, equivalently, parallel to the local wave vector, as in normal rolls^{5,6} (NRs). The

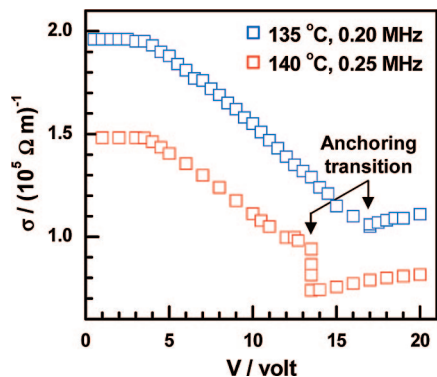


Figure 11. Voltage variation of electrical conductivity for an initially homeotropic layer of BCCB, with temperature and field frequency as constant parameters.

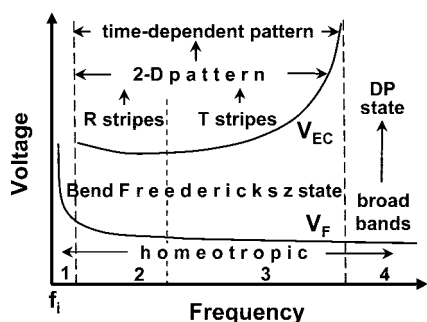


Figure 12. Schematic of the bifurcation states in the voltage-frequency space inside the conduction regime, above the dielectric isotropy point f_i for BCCB. V_F and V_{EC} denote the critical voltages for the onset of BF and electroconvective instabilities, respectively. The BF and EC patterned states in regions 2 and 3 are metastable and, over an extended time, give way to the DP state or a patterned state arising out of it. In region 4, the BF state is unstable to the formation of broad bands.

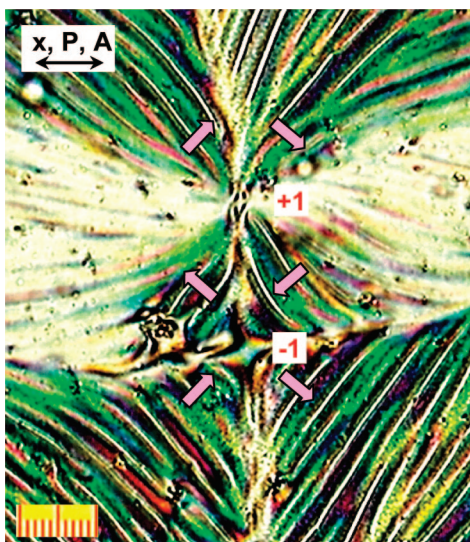


Figure 13. Pattern of periodic stripes around +1 and -1 umbilics obtained using parallel polarizers P(x)-A(x); 135 °C, 100 kHz, 16.1 V. Block arrows indicate the direction of drift of the domains. $d = 29.0 \mu\text{m}$. Scale division $10 \mu\text{m}$.

extraordinary refractive index is thus periodically modulated along a given circle centered on the defect, leading to radial focusing. In Figure 13 showing the pattern recorded with P(x)-A(x), the lines around the +1 umbilic, are accordingly well defined along y where the light vibration is extraordinary, but indistinct along x where it is ordinary. On raising V , the

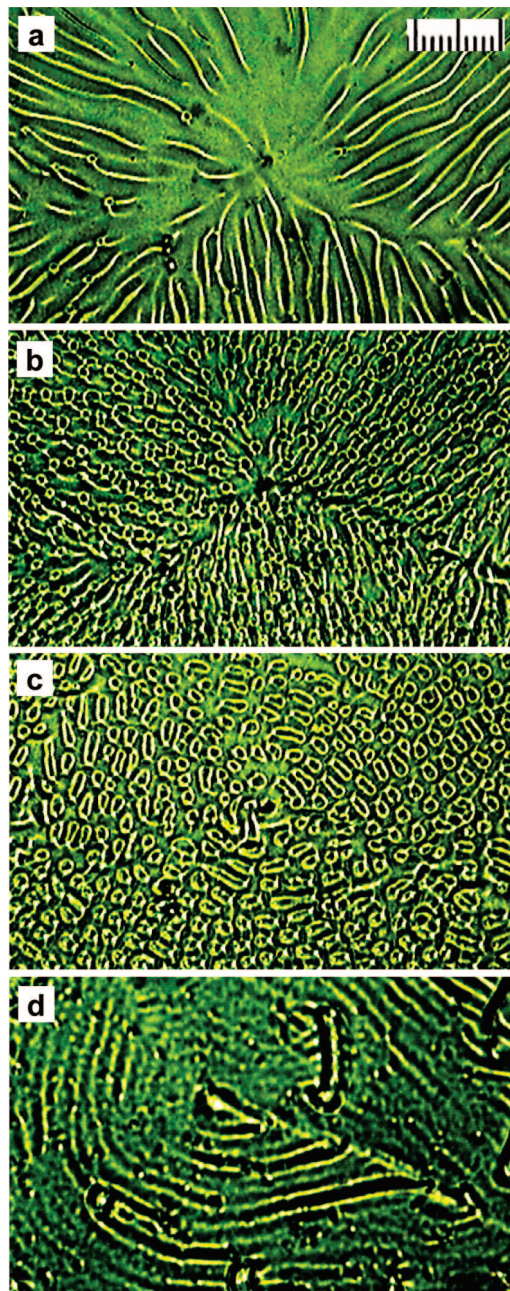


Figure 14. Sequence of transformation from the tangential to radial wave vector state (i.e., R stripes \rightarrow T stripes) under increasing frequency and constant voltage (20 V). Natural light. $f(\text{kHz}) = 190$ (a), 210 (b), 230 (c), and 260 (d). $d = 18.6 \mu\text{m}$. Scale division $10 \mu\text{m}$.

pattern first develops a cross-roll instability and thereafter becomes highly time-dependent or quasi-turbulent.

Interestingly, the radial domain instability just mentioned occurs only in a limited frequency interval of about 50 kHz at 140 °C (range 2, Figure 12). With further elevation in frequency, keeping the voltage constant, the focal lines *gradually* adopt a tangential geometry (T stripes). This distortion switch-over is illustrated in Figure 14 reproducing the textures recorded in natural light, at 140 °C and 20 V. The focal lines are purely radial in panel (a) at 190 kHz and tangential in (d) at 260 kHz; the transition between these states occurs through the formation of tiny closed domains which are, in panel (b), nearly circular and connected by radial lines, and, in (c), oblong and unconnected. When T stripes are observed using a single polarizer, the tangential focal lines lying along the vibration direction of

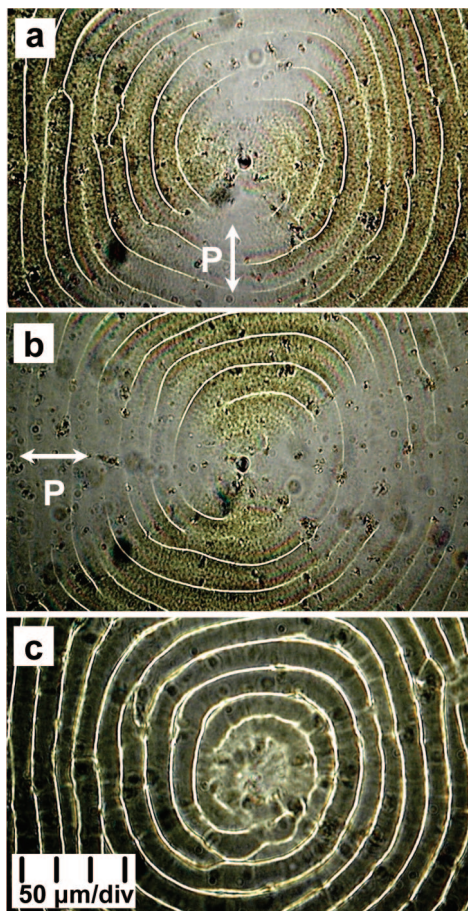


Figure 15. Periodic pattern of tangential line images formed in the BF state. Real focal plane for (a) and (b) with a single polarizer P as shown; imaginary plane and natural light for (c). 12.8 V, 125 kHz, 135 °C. $d = 29.0 \mu\text{m}$.

light appear with maximum contrast, but those transverse to this direction almost disappear, as seen in Figure 15. On the basis of this observation, two alternative models of director modulation could be considered. Before the onset of the patterned instability, the director projection in the $z = 0$ midplane for a +1 chiral umbilic may be represented as in Figure 16a. In the patterned state, the distortion may involve a periodic director twist about the radial direction as in Figure 16b, which does not alter the c -field; alternatively, c may be periodically twisted about z along any given radius (while S remains unaltered, beyond the core) as in Figure 16c. In the latter case, electrical conductivity anisotropy could lead to the generation of periodic space charges of alternating sign in the radial direction. In other words, the director field in Figure 16c may be sustained through the Carr–Helfrich (CH) mechanism of electroconvection. In fact, a similar model has recently been proposed by Stannarius and Heuer¹⁶ to explain the roll pattern with the wave vector transverse to the director easy axis evolving within the splay Freedericksz state of a phenylbenzoate–bent-core (PBBC) nematic. Their 1-D modified CH-theory predicts, for a constant effective tilt angle between 0 and $\pi/2$, a periodic state stable above a voltage threshold greater than V_F , and belonging to the conduction regime characterized by a steady director field and an oscillating charge field. However, this theory or the corresponding model in Figure 16c cannot entirely account for the texture in Figure 15 since, with a tilt that is uniform in the layer plane or with a constant magnitude S of \mathbf{n}_\perp , no focusing effects are expected; hence, near the threshold, the pattern can reveal itself only under

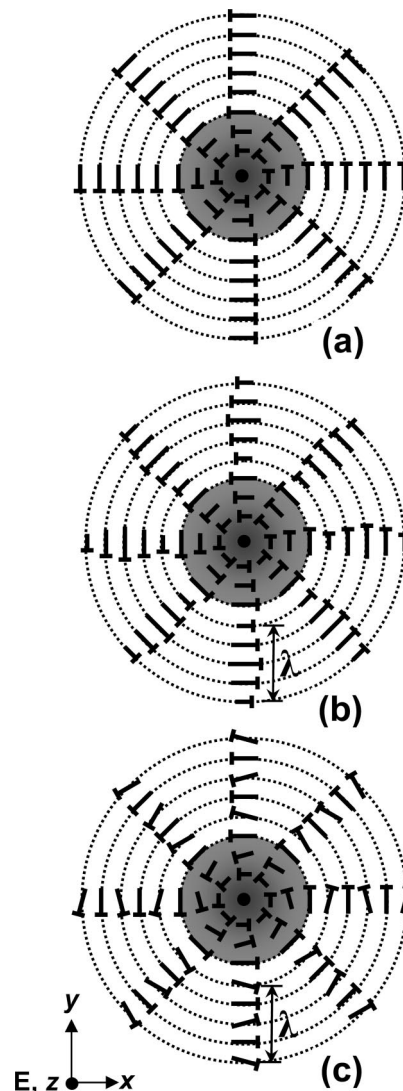


Figure 16. The director field at a +1 umbilic in the midplane $z = 0$. The shaded region represents the core within which $S = \ln|\mathbf{n}_\perp|$ approaches 0 toward the center. Beyond the core, S is assumed to be a constant in (a) for the unpatterned state. Beyond the core, in (b), a twist modulation of the director about the radial direction with unchanged c is shown; in (c), an in-plane modulation in the radial direction with a constant S is depicted.

crossed polarizers, with the maximum visibility requiring the incident vibration direction to be at a slight angle to the unmodulated c vector. While in PBBC no focalization is seen accordingly, in BCCB focal lines are observed in natural light, both in real and virtual planes, as in the WDM; Figure 15c demonstrates the striking appearance of virtual lines under unpolarized light. This feature in BCCB is accounted for in the model in Figure 16b. We are thus driven to the conclusion that the actual distortion is some combination of the director profiles provided in the two models.

We may define the dimensionless control parameter for the patterned instability by $R = (V_{\text{rms}}/V_F)^2$, as in ref 17, with the applied field given by $V(t) = E_0 d \cos(\omega t) = \sqrt{2} V_{\text{rms}} \cos(\omega t)$. The frequency variation of the threshold control parameter $R_c = (V_c/V_F)^2$ is presented in Figure 17. The diverging tendency of R_c toward the limit of the usual low-frequency conduction regime is a general feature predicted by the CH-mechanism-based theories for both planar¹⁸ and homeotropic¹⁷ initial alignments. Additionally, we have here $|\epsilon_a|$ increasing with frequency that could accelerate the rise in R_c with frequency; $\sigma_a(f)$ would

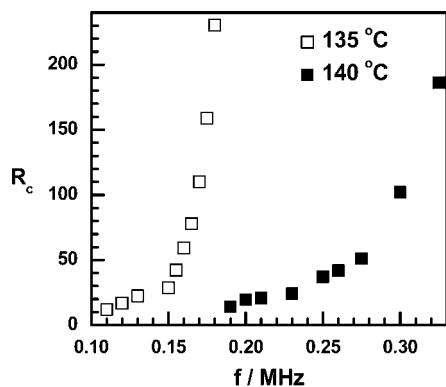


Figure 17. Frequency variation of critical control parameter R_c for electroconvection in phase 1, for two temperatures.

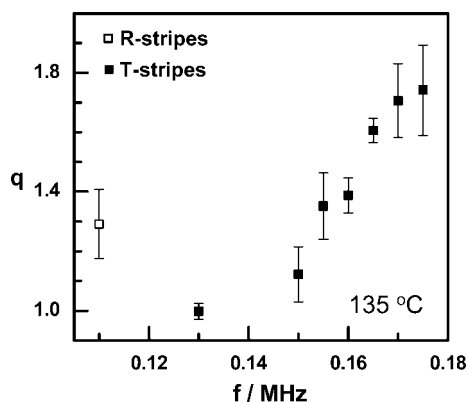


Figure 18. Frequency variation of critical wavenumber q in units of π/d for the stripe state in phase 1.

also modify the $R_c(f)$ profile, $R_c(\sigma_a)$ being a decreasing function.¹⁷ It is relevant to note here that the theoretical stability analysis in ref 10 for the homeotropic geometry and high frequency regime ($f-f_i$) predicts the pattern threshold to continuously decrease with increasing frequency, but we find an opposite trend in BCCB.

In Figure 18, the frequency dependence of the threshold wavenumber q , expressed as a dimensionless quantity in units of π/d , is presented for 135 °C. As it happens, the domain line geometry switches from radial to tangential at ~ 0.13 MHz, and all the data points shown by the solid squares in the figure correspond to the T-stripes instability. They show that q rises ever more rapidly with increasing f . Although the director field for the tangential domains differs significantly from that for the usual NRs, the extended CH theory for the latter in $(-\varepsilon_a, +\sigma_a)$ nematics with homeotropic initial alignment predicts¹⁷ a variation of $q(f)$ similar to that in Figure 18.

At higher values of R , the pattern of tangential stripes formed at R_c changes into a bimodal or 2-D structure as illustrated in Figure 19. At this stage, phase 1 becomes short-lived, and phase 2 takes over in a matter of seconds; in Figure 19, phase 2, which is advancing from the left, is in a state far from the primary pattern threshold, displaying a chevron texture.

In the high-frequency region (>400 kHz, 140 °C), the BF state becomes unstable to a patterned instability comprising periodic broad domains as in Figure 20a. The structure now involves variations mainly in the azimuthal angle φ . For ease of discussion, the rectangular region outlined within Figure 20a is shown enlarged in panel (b); (c) depicts the same region for $P(x)-A(y)$. The birefringent bands in (b) are designated B_s or B_u , the subscripts s and u describing the speckled and uniform textures, respectively. The manifestation of director fluctuations

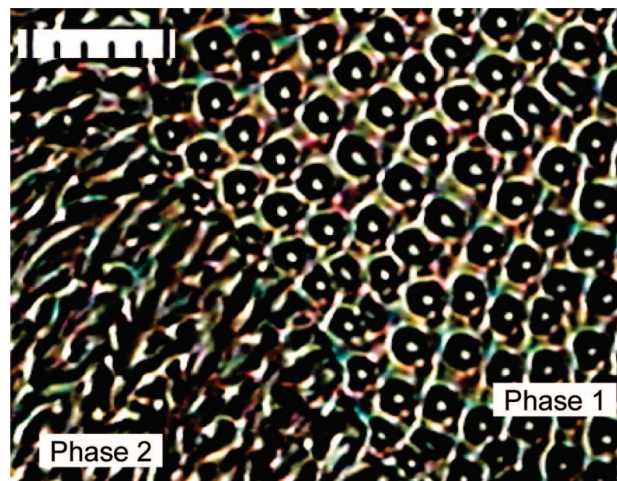


Figure 19. Right: 2-D pattern observed at a +1 umbilic in phase 1. Left: Chevron state of phase 2. $P(x)-A(y)$, 135 °C, 150 kHz, 17.7 V. $d = 14.7 \mu\text{m}$. Scale division $10 \mu\text{m}$.

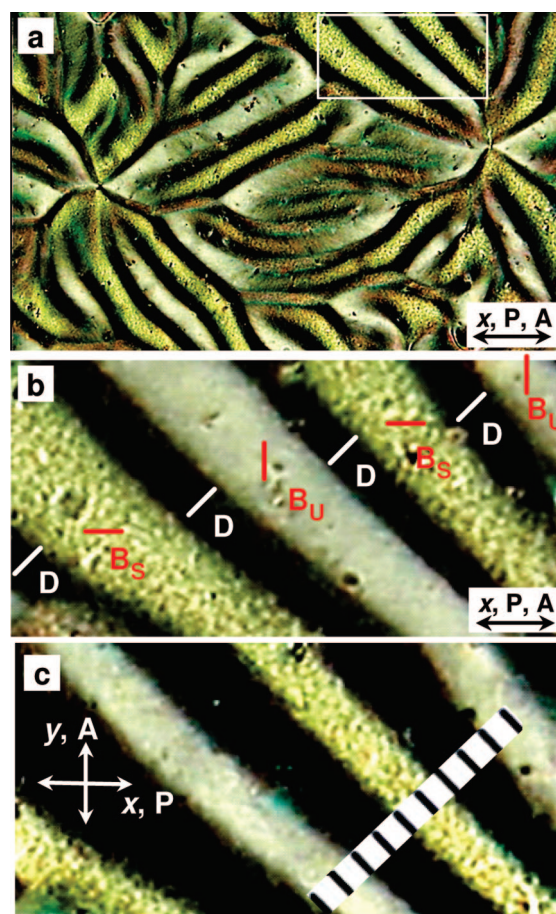


Figure 20. The broad domain texture formed in the very high frequency regime of phase 1. Pattern period $\lambda \sim 4.5d$. 400 kHz, 10.6 V, 140 °C. (b) and (c) are enlargements of the inset area in (a). $d = 18.9 \mu\text{m}$. Scale division $10 \mu\text{m}$.

in B_s implies the \mathbf{c} vector to be predominantly along the x direction. Lack of it in B_u indicates the corresponding \mathbf{c} to be mainly along y . Clearly, the light from B_s and B_u regions becomes extinct under $P(x)-A(y)$, as seen in (c). In the region of dark bands D in (b), if we take the director to be at 45° to x as indicated, the emergent light has to be linearly polarized along y to be blocked by a parallel polarizer. Ideally, this implies a phase difference that is an odd integral multiple of π . Then,

between crossed polarizers as in (c), the corresponding regions should appear identically bright; however, they are alternately speckled and uniform, and this could mean a slight, alternately positive and negative director deviation from the idealized diagonal orientation shown.

The observation of the broad domain mode (BDM) in highly conducting nematics in the usual conduction regime has a long history.^{19–22} Broad domains involve the same kind of spatial symmetry breaking as chevron patterns, a spatially periodic in-plane rotation of the *c* director. But while the formation of chevron patterns from the defect chaotic state of convection in either the dielectric or the conduction mode has been understood by a coupling of the topological charges with the Goldstone mode,²³ the discussion of the origin of broad domains,^{23–26} which are, at higher voltages, often superimposed with convection rolls and eventually develop into defect-free form of chevrons,²² has remained inconclusive. The broad domains in BCCB are somewhat similar to the prewavy domains described by Huh et al.²¹ and formed in the BF state of a calamitic mesogen (MBBA). Particularly the domain periods in the two cases are comparable ($\lambda \sim 4–6d$). However, the organized vortex flows (both in-layer and across-layer flows), indicated by tracer particle trajectories in MBBA, are not found in our case. In fact, the absence of coherent dust-particle motion in BCCB precluded our ascertaining whether the instability operated into the isotropic state, as in the case of the prewavy mode. Thus it is also possible that the broad domains here belong to the inertial branch of the CH instability. There is also a suggestion that the WDM may emerge as a solution of coupled amplitude equations appropriate to the stationary roll pattern and a homogeneous mode describing the in-layer director orientation.²⁷

In the end, two aspects relating to the dynamics of the instabilities need mentioning. First, we could not detect any organized motion of dust particles through which to infer the existence of cellular flows. This might mean a rather weak electroconvection as envisaged by Chigrinov et al.¹¹ for the striped pattern state in some rod-like nematics occurring in a narrow frequency band spreading across the dielectric isotropy point. Second, all the patterns display a steady drift and, as an example, we have indicated the drift direction by block arrows in Figure 13 (see Supporting Information for a movie clip of drift). In every case, the direction of drift coincides with the easy director axis in the layer plane. The drift phenomenon is common to the patterns in phase 2 as well. We have made a systematic study of this propagative instability in phase 2 and will deal with it separately.

Conclusions

We have explored the homogeneous and patterned states that occur in an electrically driven, homeotropically aligned, bent-core-calamitic nematic, in the frequency regime beyond the dielectric inversion point. Periodic distortions arise as secondary instabilities at the umbilical defect sites formed during the BF transition. Under increasing frequency, the first of the patterned states manifests optically as Williams-like (standard) striations corresponding to the wave vector along the local easy axis; then a pattern transformation follows such that the wave vector orients transverse to the easy axis (nonstandard state). The striations, which are the focal lines observable in natural light, may be understood on the basis of the CH model (standard striations) or one of its adaptations (nonstandard striations). Finally, in the high frequency region, regularly spaced broad

bands form, which are best observed using slightly uncrossed polarizers and which involve periodic azimuthal deviations. A novel feature of the patterned states is the sustained propagative instability they exhibit. We have found it convenient to examine this drift in detail in the DP state to which the metastable BF state transforms. We have described and discussed the instabilities pertaining to the DP state in a separate paper.²⁸

Acknowledgment. We thank Professor K. A. Suresh for his keen interest in this investigation. P.K. acknowledges support from the Council of Scientific and Industrial Research, India.

Supporting Information Available: A video clip of the drifting pattern of stripes demonstrating tangential clockwise motion around +1 umbilic, and radial inward and outward motions in the two sets of opposite quadrants centered at –1 umbilic; 160 kHz, 18.3 V, 135 °C, crossed polarizers. This material is available free of charge via the Internet at <http://pubs.acs.org>.

References and Notes

- (1) de Jeu, W. H.; Gerritsma, C. J.; van Zanten, P.; Goossens, W. J. A. *Phys. Lett.* **1972**, *39A*, 355.
- (2) de Jeu, W. H.; Lathouwers, Th. W. *Mol. Cryst. Liq. Cryst.* **1974**, *26*, 335.
- (3) Blinov, L. M.; Chigrinov, V. G. *Electrooptic Effects in Liquid Crystal Materials*; Springer: Berlin, 1994.
- (4) Pikin, S. A. *Structural Transformations in Liquid Crystals*; Gordon and Breach Science Publishers: New York, 1991.
- (5) Kramer, L. In *Pattern Formation in Liquid Crystals*; Buka, A., Kramer, L., Eds.; Springer: Berlin, 1996.
- (6) de Gennes, P. G.; Prost, J. *The Physics of Liquid Crystals*; Clarendon Press: Oxford, 1993.
- (7) Goossens, W. J. A. *Phys. Lett.* **1972**, *40A*, 95.
- (8) Dubois-Violette, E.; de Gennes, P. G.; Parodi, J. *J. Phys. (Paris)* **1971**, *32*, 305.
- (9) Gerber, P. R. *J. Phys. (Paris)* **1985**, *46*, 1865.
- (10) Chigrinov, V. G.; Korkishko, T. V.; Barnik, M. I.; Trufanov, A. N. *Mol. Cryst. Liq. Cryst.* **1985**, *129*, 285.
- (11) Chigrinov, V. G.; Sparavigna, A.; Strigazzi, A. *Phys. Rev. E* **1996**, *53*, 4918.
- (12) Yelamagad, C. V.; Krishna Prasad, S.; Nair, G. G.; Shashikala, I. S.; Shankar Rao, D. S.; Lobo, C. V.; Chandrasekhar, S. *Angew. Chem., Int. Ed.* **2004**, *43*, 3429.
- (13) (a) Rapini, A. *J. Phys. (Paris)* **1973**, *34*, 629. (b) Rapini, A.; Leger, L.; Martinet, A. *J. Phys. (Paris)* **1975**, *36*, C1-189.
- (14) Stannarius, R.; Eremin, A.; Tamba, M.-G.; Pelzl, G.; Weissflog, W. *Phys. Rev. E* **2007**, *76*, 061704.
- (15) Morris, S. W.; Palffy-Muhoray, P.; Balzarini, D. A. *Mol. Cryst. Liq. Cryst.* **1986**, *139*, 263.
- (16) Stannarius, R.; Heuer, J. *Eur. Phys. J. E* **2007**, *24*, 27.
- (17) Hertrich, A.; Decker, W.; Pesch, W.; Kramer, L. *J. Phys. II (Paris)* **1992**, *2*, 1915.
- (18) Bodenschatz, E.; Zimmermann, W.; Kramer, L. *J. Phys. (Paris)* **1988**, *49*, 1875.
- (19) Ribotta, R.; Durand, G. *J. Phys. (Paris)* **1979**, *40*, C3–334.
- (20) Trufanov, A. N.; Blinov, L. M.; Barnik, M. I. *Sov. Phys. JETP* **1980**, *51*, 314. (a) A novel type of the electrohydrodynamic instability in nematic liquid crystals. In *Advances in Liquid Crystal Research and Applications*; Bata, L., Ed.; Pergamon Press, Oxford, 1980; pp 549–560.
- (21) Huh, J.-H.; Yusuf, Y.; Hidaka, Y.; Kai, S. *Phys. Rev. E* **2002**, *66*, 031705.
- (22) Huh, J.-H.; Hidaka, Y.; Rossberg, A. G.; Kai, S. *Phys. Rev. E* **2000**, *61*, 2769.
- (23) Rossberg, A. G.; Kramer, L. *Physica D* **1998**, *115*, 19.
- (24) Pikin, S. A.; Chigrinov, V. G. *Sov. Phys. JETP* **1980**, *51*, 123.
- (25) Blinov, L. M.; Barnik, M. I.; Trufanov, A. N. *Mol. Cryst. Liq. Cryst.* **1982**, *89*, 47.
- (26) Rossberg, A. G. *Phys. Rev. E* **2000**, *62*, 8114.
- (27) Komineas, S.; Zhao, H.; Kramer, L. *Phys. Rev. E* **2003**, *67*, 031701.
- (28) Pramoda, K.; Hiremath, U. S.; Yelamagad, C. V.; Rossberg, A. G.; Krishnamurthy, K. S. *J. Phys. Chem. B*, in press.